Research Article

Mario Marini, Margaux Bouzin*, Riccardo Scodellaro, Laura D'Alfonso, Laura Sironi, Francesca Granucci, Francesca Mingozzi, Giuseppe Chirico, Maddalena Collini

Quantitative active super-resolution thermal imaging: The melanoma case study

https://doi.org/10.1515/bmc-2022-0015
received January 30, 2022; accepted March 10, 2022

Abstract: Super-resolution image acquisition has turned photo-activated far-infrared thermal imaging into a promising tool for the characterization of biological tissues. By the sub-diffraction localization of sparse temperature increments primed by the sample absorption of modulated focused laser light, the distribution of (endogenous or exogenous) photo-thermal biomarkers can be reconstructed at tunable ~10–50 μm resolution. We focus here on the theoretical modeling of laser-primed temperature variations and provide the guidelines to convert super-resolved temperature-based images into quantitative maps of the absolute molar concentration of photo-thermal probes. We start from camera-based temperature detection via Stefan–Boltzmann's law, and elucidate the interplay of the camera point-spread-function and pixelated sensor size with the excitation beam waist in defining the amplitude of the measured temperature variations. This can be accomplished by the numerical solution of the three-dimensional heat equation in the presence of modulated laser illumination on the sample, which is characterized in terms of thermal diffusivity, conductivity, thickness, and concentration of photo-thermal species. We apply our data-analysis protocol to murine B16 melanoma biopsies, where melanin is mapped and quantified in label-free configuration at sub-diffraction 40 μm resolution. Our results, validated by an unsupervised machine-learning analysis of hematoxylin-and-eosin images of the same sections, suggest potential impact of super-resolved thermography in complementing standard histopathological analyses of melanocytic lesions.

Keywords: infrared thermography, super-resolution imaging, melanoma, hematoxylin-and-eosin stain, k-means clustering

Introduction

Temperature and externally induced temperature variations provide a powerful imaging contrast agent. A number of well-established techniques indeed rely on temperature for the quantitative investigation of the morphology and functional state of biological samples [1–7]. Temperature is typically probed indirectly, either through the response of optical properties, such as reflectance [8] and index of refraction [4–6], to a modulated change in the sample temperature, or by the quantification of the sample thermal radiation in the infrared spectral band [9,10]. The latter approach is at the basis of (far) infrared thermography, and enables a conceptually straightforward retrieval of absolute temperature values: a thermal camera senses the sample surface infrared radiance R, which is subsequently converted into an absolute temperature T by Stefan–Boltzmann's law ($R = \epsilon\sigma T^4$, where $\sigma = 5.67 \times 10^{-8}$ Wm^{-2} K^{-4} is Stefan–Boltzmann's constant) under the assumptions of grey-body radiance and known sample emissivity ϵ [9,10].

With the main advantages of quantitative and non-contact temperature measurements over variably extended (>mm^2 sized) sample areas, infrared thermography is nowadays a well-established technology and finds promising applications in the life sciences [2,11]. In fact, information on the alterations and structural properties of biological tissues can be recovered by exploiting heat transfer processes [1,2,11,12]. For example, the spatial distribution of photo-thermal biomarkers (e.g., melanin in melanoma skin lesions [5]) could be obtained by photo-activated thermal imaging

* **Corresponding author: Margaux Bouzin,** Physics Department, Università degli Studi di Milano-Bicocca, Piazza Della Scienza 3, 20126, Milano, Italy, e-mail: margaux.bouzin@unimib.it
Mario Marini, Riccardo Scodellaro, Laura D'Alfonso, Laura Sironi: Physics Department, Università degli Studi di Milano-Bicocca, Piazza Della Scienza 3, 20126, Milano, Italy
Francesca Granucci, Francesca Mingozzi: Biotechnology and Biosciences Department, Università degli Studi di Milano-Bicocca, Piazza Della Scienza 2, 20126, Milano, Italy
Giuseppe Chirico, Maddalena Collini: Physics Department, Università degli Studi di Milano-Bicocca, Piazza Della Scienza 3, 20126, Milano; CNR Institute for Applied Science and Intelligent Systems, Via Campi Flegrei 34, 80078, Pozzuoli, Italy

experiments on biopsy specimens, thereby leading to the development of novel protocols aimed at the screening and early-stage detection of pathologies. Similarly, in the field of precision medicine, where light-responsive (nano-) regulators have gained increased attention [13] to manipulate cell functions, active thermography can map the biodistribution of photothermal probes in both superficial tissues and biopsies of the main organs involved in the accumulation process [14]. For all these applications, (i) imaging at high (~1–50 μm) spatial resolution and (ii) the possibility of extracting quantitative information (e.g., the sample thermal properties [15] and the concentration of photo-thermal probes [16]) from the detected temperature variations represent important issues and the major challenges to face.

The spatial resolution of commercially available far-infrared microbolometer-based cameras is theoretically limited to ~0.1–0.5 mm due to diffraction at the typically low numerical aperture of the collecting Germanium optics (Abbe's law [17,18]). Such a nominal resolution is further worsened to ~1 mm by the extended camera pixel size on the sample plane and by the thermal wave diffusion in the sample, which turns the effective imaging resolution into an increasing function of time. Irrespective of the nominal resolution of the adopted thermal camera, the theoretical diffraction barrier can be overcome by the implementation of super-resolution image acquisition schemes [14,19]. By exploiting a modulated raster-scanned laser illumination of the sample, coupled to the *a-posteriori* localization of the resulting laser-induced temperature variations in the camera frames, we have recently demonstrated that light-absorbing and heat-releasing entities in the sample can be identified with a resolution that is only assigned by the number of photons detected in each temperature peak and by the excitation laser beam waist [14]. The visible laser waist can be reduced up to its ~1-μm diffraction-limited size, and temperature mapping can be routinely performed at a tunable ~40 μm spatial resolution with typical detected temperature increments of few degrees [14].

However, in the simplest implementation of super-resolution thermography, while the peak coordinates of laser-primed temperature increments assign the location of photo-thermal entities in the reconstructed image of the sample, the amplitude of temperature variations is only exploited to define the image false-color code [14]. The sample thermal conductivity can be measured by exploiting the temperature rise-and-decay temporal kinetics under modulated laser illumination [15]; by contrast, no quantitative information on the concentration of absorbing and heat releasing entities is retrieved [14].

In a view of fully exploiting the information encoded in the super-resolved temperature-based image of a biological tissue, we complement our super-resolution imaging approach [14,15] with the necessary theoretical framework to model experimentally detected temperature increments as a function of both instrumental parameters and the concentration of laser-excited photo-thermal probes. Provided that temperature heterogeneities in super-resolution imaging experiments typically occur close to (or even below) the spatial scale of individual camera pixels, we especially focus on the tight interplay of the camera response function (the diffraction-limited widening of a point source point-spread-function [PSF]), the camera pixelated sensor size, and the excitation laser beam waist in defining the amplitude of the measured temperature variations. Based on the solution of the three-dimensional heat transfer model in the presence of laser light illumination [20] and camera-based temperature detection, we outline the general guidelines and formalism to convert an exclusively morphological thermal map into a quantitative image of the concentration of laser-excited photo-thermal probes.

We validate our results and demonstrate a biologically relevant exemplary application with the non-destructive characterization of the spatial distribution and absolute molar concentration of melanin pigments in excised murine melanoma biopsies. By taking advantage of the endogenous photo-thermal effect primed by melanin absorption of focused 514 nm laser light, we spatially map melanin pigments in label-free configuration at sub-diffraction 40 μm resolution, and provide the data analysis protocol to retrieve the absolute pigment concentration with 10^{-4} M sensitivity. The space-resolved quantification of the melanin concentration is further strengthened with a lightness-based [21] *k*-means clustering algorithm [22] of hematoxylin-and-eosin (H&E) images [23] of the same tissue sections, and retains biological relevance in complementing the immuno-histochemical and morphological features that are traditionally extracted from the standard histopathological visual inspection of H&E-stained sections. Provided the still debated but crucial role played by melanin and altered melanogenesis in the overall development and evolution of melanoma [24–27], the melanin concentration is regarded as a promising marker for melanoma diagnosis by pathologists [25,28]. We expect therefore the proposed super-resolution photo-thermal imaging method to quantitatively complement traditional histopathology in the characterization of pigmented lesions *ex-vivo*.

Materials and methods

Super-resolution far-infrared thermography: principles and experimental setup

Our recently developed super-resolution photo-thermal imaging scheme [14,15] shares some of the working principles of the fluorescence-based super-resolution techniques of Photo-Activated Localization Microscopy (PALM) [29] and Stochastic Optical Reconstruction Microscopy (STORM) [30]. We take advantage of a photo-activated configuration of thermal imaging, where a focused low-power visible/near-infrared laser beam is raster-scanned and modulated in time to sparsely prime the photo-thermal effect (light absorption and thermal relaxation) inside the sample. The resulting sequence of isolated temperature increments is imaged by a far-infrared thermal camera, and the automated non-linear surface Gaussian fit of the individual thermal camera frames is exploited to retrieve the peak amplitude $\overline{\Delta T}_{max}$ of each temperature variation, as well as the center coordinates of the corresponding light-absorbing and heat-releasing entity. The super-resolved image of the sample is finally reconstructed *a-posteriori* based on the localized positions of the absorptive centers, with the false color-code assigned by the amplitudes of temperature increments. The resolution in the localization of photo-thermal components is only determined by (i) the signal-to-noise ratio of the fitted frames and (ii) the excitation laser spot size, ideally down to its diffraction-limited ~1-μm size at the employed visible to near-infrared wavelength.

Super-resolution thermography experiments are performed here on a custom-made benchtop optical setup [14]. The photo-thermal effect is primed by a continuous-wave Argon laser beam (λ_{exc} = 514 nm, $1/e^2$ beam radius ω = 30 μm, and P_0 = 33 mW on the sample plane; Spectra Physics, CA, USA) which is scanned across the sample via a scanning unit (a two-lens scan system with 4 and 10 cm focal lengths, followed by a 10 cm lens for beam focalization onto the sample plane) coupled to two galvanometric mirrors (MicroMax Series 670, Cambridge Technology Inc., MA, USA). A programmable board (LabVIEW RIO, National Instruments, TX, USA) operates the mirrors in raster-scanning mode on a $N_x x N_y$ grid with adjustable pixel size δx on the sample plane. To ensure the detection of one temperature peak at a time (which significantly simplifies image fitting and the peak localization procedure), an electronic shutter (Oriel 76992, Newport, CA, USA) is synchronized with the laser scan to modulate the illumination in time. During each raster scan, laser illumination (open shutter condition) is only allowed on a subset of pixels lying at distances Δx and Δy along the x- and y-directions. Δx and Δy are selected to guarantee that a minimum spatial and temporal distance occurs between consecutively induced temperature increments. Provided that $\Delta x \cdot \Delta y$ consecutive scans are required to illuminate the whole region of interest once, the total imaging time lies in the 10–200 min range depending on N_x, N_y, Δx, Δy and on the laser pixel dwell time. By default, during shutter closure, the laser is scanned with a pixel dwell time τ_{off} = 6 ms; whenever the laser illumination has to be allowed on the sample plane, the shutter is opened for a time interval τ_{on} = 0.2 s and the corresponding pixel dwell time is temporarily increased to the same value.

An uncooled microbolometer-based thermal camera (FLIR T650sc, FLIR Systems Inc., OR, USA; 7.5–13 μm spectral detection band, 640 × 480 sensor format, and 30 Hz frame rate) detects the thermal radiation in reflection configuration with numerical aperture N.A. = 0.023 and 420-μm pixel size on the sample plane at a minimum 40 cm camera-to-sample distance. Based on Abbe's diffraction law [18], the theoretical limit to the camera resolution (computed as the full-width-at-half-maximum ζ of the camera PSF) is 0.6 λ/N.A. = 0.26 mm at the central 10-μm wavelength of the spectral detection band. Experimentally, the spatial resolution is worsened by both the extended camera pixel size on the sample plane and the thermal wave diffusion; as long as heat propagates across the sample, heat diffusion increasingly worsens the imaging resolution and turns it into an increasing function of time. Overall the far-infrared thermography setup conventionally operates at a typical ~1 mm spatial resolution [14], and necessarily requires super-resolution image acquisition when applied to the investigation of biological samples on the tissue spatial scale.

For melanin pigments in murine melanoma biopsies, the emissivity has been set to ϵ = 0.98 according to the literature [31].

Transmission microscopy setup

Transmitted-light images of murine B16 melanoma biopsies have been acquired on a TCS SP5 STED-CW confocal microscope (Leica Microsystems, D). A 633 nm He–Ne beam with 10 μW power on the sample plane is focused by a 20× 0.5-N.A. air objective (HCX PL Fluotar, Leica Microsystems, D), and transmitted light is collected by a non-spectral dedicated photo-multiplier tube with no confocal pinhole along the detection optical path. Whole biopsies (up to cm^2 in size) have been imaged in mosaic

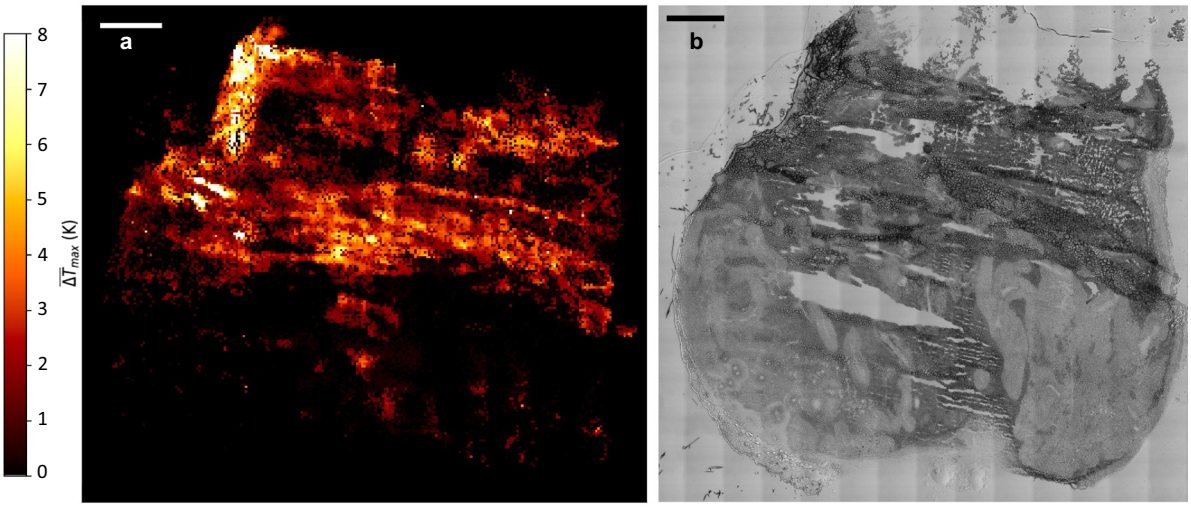

Figure 1: B16 melanoma biopsy imaged by super-resolution photo-activated thermography. (a) Super-resolved photo-thermal image of an unstained murine B16 melanoma biopsy; λ_{exc} = 514 nm, P_0 = 33 mW, τ_{on} = 0.2 s, ω = 28 µm , δx = 37.8 µm, and scale bar = 1 mm. Black color codes for pixels where no photo-thermal signal has been detected above the 0.1 K sensitivity of the thermal camera. (b) Transmitted-light image of the same biopsy imaged in (a); scale bar = 1 mm.

(tile-scan) mode with 400 Hz raster scan frequency per line.

B16 biopsies

The murine tumor B16 cell line has been cultured in IMDM-10 complete medium (10% heat-inactivated FBS, 2 mM L-glutamine, 100 U/mL penicillin, and 100 µg/mL streptomycin), and a tumorigenic dose of 2×10^6 cells at 70% confluence has been injected in the deep derma of the left flank of C57bl/6 mice at 7–12 weeks of age. Tumors have been collected from euthanized mice 14 days after cells injection, and explanted tissues have been cut in 20 µm sections on a cryostat upon embedding in OCT freezing medium (Bio-Optica, I). Sections have been adhered to 1 mm glass slides (Superfrost Plus, Thermo Fisher Scientific, MA, USA). Upon completion of super-resolution photo-thermal imaging, the same sections have been stained with H&E. Sections have been immersed in Meyer's hematoxylin solution for 8 min and washed for 5 min in running water; they have been immersed in Eosin Y solution for 1 min, washed in running water, rinsed in distilled water, and dehydrated with passages in 95% and absolute alcohol. Slides have been cleared in xylene and mounted with Eukitt. A NanoZoomer scanner (Hamamatsu, JP) has been employed for the acquisition of H&E images.

All the experiments have been performed under protocols approved by the Institutional Animal Care and Use Committee of Università degli Studi di Milano-Bicocca and the Italian Ministry of Health.

Finite-element simulations

Finite-element simulations have been performed by COMSOL Multiphysics (Comsol AB, SE) based on the built-in heat transfer module. The Gaussian-shaped excitation laser source has been implemented as a square-wave pulse lasting τ_{on} = 0.2 s, with 30-µm $1/e^2$ beam radius, and adjustable power as employed in super-resolution imaging experiments. Two-layer samples – mimicking imaged melanoma biopsies – have been modeled as a 20-µm thick skin layer (k = 0.37 $Wm^{-1}K^{-1}$, $D = 9.84 \times 10^{-8}\,m^2/s$) overlaid to a 1 mm thick glass substrate (k = 0.9 $Wm^{-1}K^{-1}$, $D = 5.02 \times 10^{-7}\,m^2/s$), whereas single-layer samples have been simulated as a 1,020-µm thick cylindrical glass slab. The comparison of the temporal evolution of the amplitude of simulated laser-induced temperature increments in the two cases has been exploited to (i) validate the equivalency of the double-layer glass + tissue sample subject to a laser power P_0 to the single-layer glass slab subjected to an increased effective laser power $P_{eff} = 1.2P_0$ as described in the text with Figure 2, and (ii) to quantify the ratio $P_{eff}/P_0 = 1.2$, which is assigned by the 20-µm and 1-mm thicknesses and by the thermal conductivity and diffusivity of the glass and skin layers, respectively. Convective and radiative heat losses have been simulated with a convective heat transfer coefficient h = 10 $W/m^2\,K$ (as typically adopted for samples

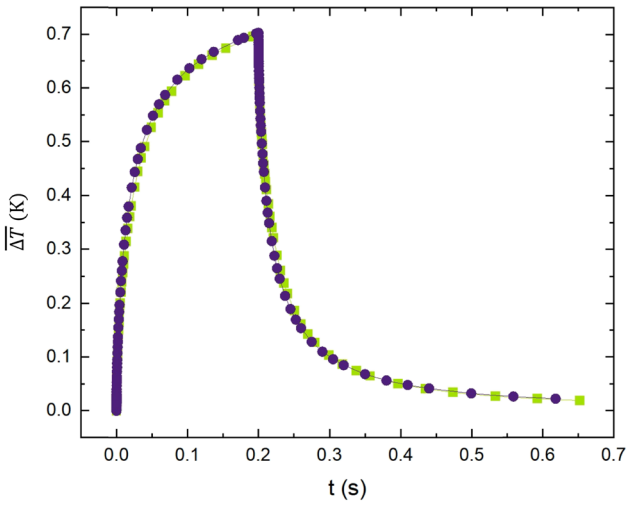

Figure 2: Finite-element simulations. Green: temporal evolution of the amplitude of the temperature increment primed on a 20 µm skin tissue section (k = 0.37 Wm^{-1} K^{-1}, D = 9.84 × 10^{-8} m^2/s) overlaid to a 1,000 µm glass slab (k = 0.9 Wm^{-1} K^{-1}, D = 5.02 × 10^{-7} m^2/s) with ω = 30 µm, τ_{on} = 0.2 s, and laser power P_0 = 0.5 mW. Violet: temporal evolution of the amplitude of the temperature increment primed on a single-layer 1,020 µm glass slab (k = 0.9 $Wm^{-1}K^{-1}$, D = 5.02 × 10^{-7} m^2/s) with ω = 30 µm, τ_{on} = 0.2 s, and effective laser power P_{eff} = 1.2 P_0 = 0.6 mW. The laser power acts as a direct proportionality constant on the amplitude of the temperature variation, therefore, the ratio P_{eff}/P_0 = 1.2 has been determined as the ratio (at any time point) of the two temperature increments simulated on the double- and single-layer samples at identical laser power. In order to simulate camera-based temperature detection, temperature values are the result of a spatial average of the simulated temperature distribution (elevated to the fourth power based on Stefan–Boltzmann's law) over a square pixel with 420 µm side as described in the text.

immersed in air at standard conditions [20,32]) and a sample emissivity ϵ = 0.98. No significant difference has been observed between temperature profiles simulated in the presence and absence of convective and radiative losses, which have therefore been neglected in equation (1).

Due to the overall axisymmetric properties of the system, cylindrical samples have been modeled as a 2D rectangle and the 3D temperature profile has been generated by rotation with significant reduction in the computational time. A triangular mesh has been employed for all the simulations with minimum element size of 80 nm and maximum element size of 10 µm.

k-means clustering

A color-based algorithm has been developed to automatically perform a semantic segmentation of the melanin content in B16 melanoma biopsies based on the corresponding 8-bit RGB-format H&E images. At first, background pixels in the image get identified by selecting a white-based threshold: each pixel is classified as a background pixel whenever all its red, green, and blue (R,G,B) channels exceed a minimum value of 220. Remaining pixels are analyzed by exploiting the iterative k-means clustering technique described in ref. [22]. k-means clustering is an unsupervised machine-learning technique that acts in the features space by minimizing the elements distance from the cluster centroids. In the first step, the user selects the k desired number of clusters (here k = 2), and the algorithm randomly identifies k points in the feature space as starting centroids. Each pixel is associated with the nearest centroid based on the Euclidean distance of the (R,G,B) color components of the pixel and of the centroid, and two different clusters are obtained. The new centroids of the two clusters are calculated, and each pixel is re-associated with the nearest centroid. The iterative process continues until the method reaches convergence and no elements are switched to different clusters. Then, the lightness parameter is retrieved for each pixel as defined in ref. [21], and the mean lightness is computed for two different clusters to discard the one with the highest mean lightness (lower melanin content is expected in pixels with higher lightness). The whole procedure is applied again on the pixels of the selected cluster, and iterated until the difference between the mean lightness parameter computed for the two clusters falls below a selected threshold (here 5% of the maximum possible lightness): at this point (nth iteration), the two clusters are not separated any more, and the pixels of the cluster surviving the (n – 1)th iteration are segmented to evidence melanin-rich regions in the H&E image.

Data acquisition and analysis software

The software FLIR Tools + (FLIR Systems Inc., OR, USA) has been employed for the acquisition of raw thermocamera images. Image sequences have been exported in .csv file format and entirely processed by a custom-written Python code. Simulated datasets in Figures 3 and 4 have been generated by a custom Python code, which performs the numerical integration of the solution of the three-dimensional heat equation (equations (1–2)) by the built-in Scipy integration routine. For Figure 5, the 2-means clustering on H&E-stained sections has been carried out on a custom-written MATLAB code.

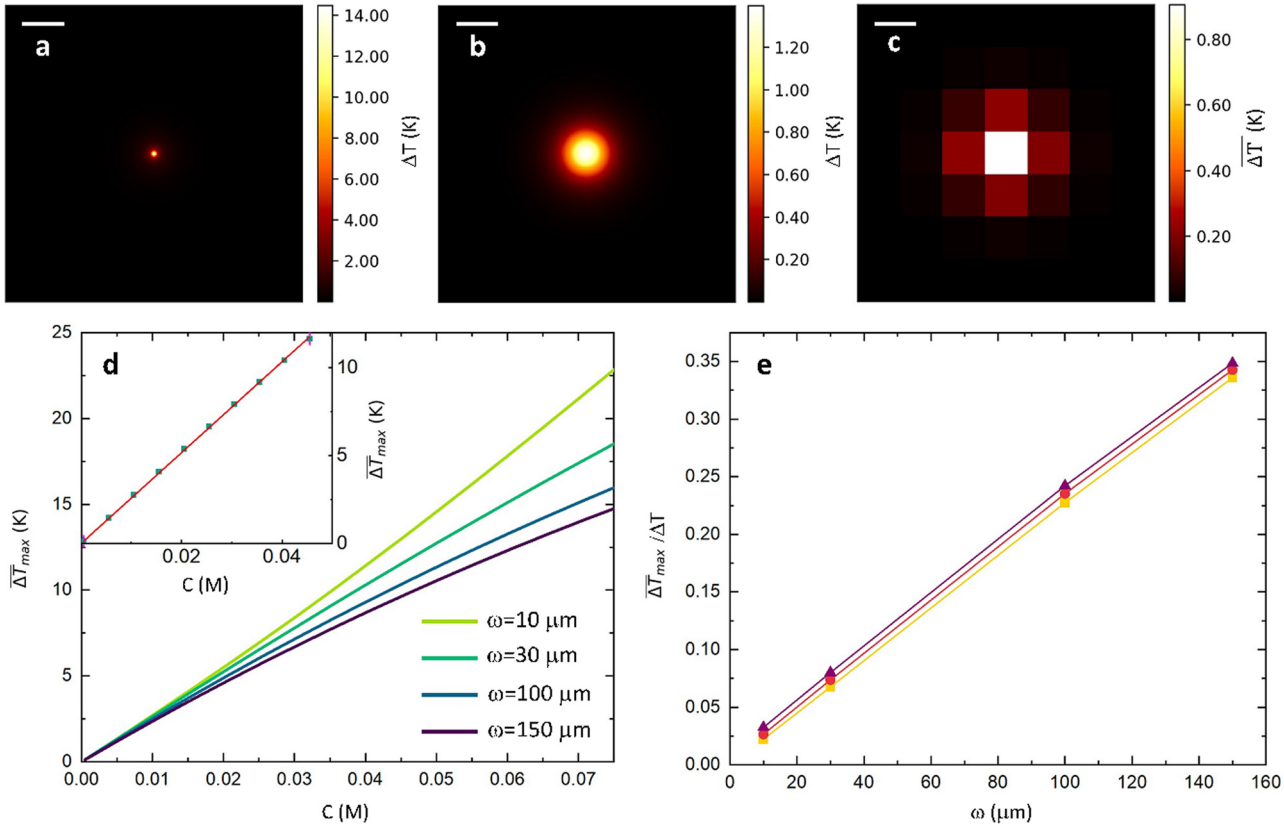

Figure 3: Quantification of the concentration of photo-thermal probes by super-resolved photo-activated thermography. (a) Temperature profile $\Delta T = T(x, y, 0, \tau_{on}) - T_0$ predicted by the numerical integration of equation (1) for ω = 30 μm, 1-mW absorbed power, τ_{on} = 0.2 s, k = 0.9 Wm^{-1} K^{-1}, $D = 5.02 \times 10^{-7}$ m^2/s. (b) Convolution of the temperature profile of panel (a) with a Gaussian camera PSF with full-width-at-half-maximum ζ = 265 μm. (c) PSF-convoluted and pixel-averaged temperature profile computed by spatially averaging the temperature increment of panel (b) over square pixels of side d = 420 μm based on equation (2). Scale bar = 420 μm for (a)–(c). (d) Dependence of $\overline{\Delta T}_{max}$ values on the concentration C of photo-thermal entities predicted by the numerical integration of equations (1) and (2) at fixed d = 420 μm and varying excitation laser beam waist ω = 10–150 μm (τ_{on} = 0.2 s, P_{eff} = 39 mW, k = 0.9 Wm^{-1} K^{-1}, $D = 5.02 \times 10^{-7} m^2/s$, ℓ = 20 μm, E = 1,500 M^{-1} cm^{-1}, and ϕ = 0.99). Inset: best linear fit to $\overline{\Delta T}_{max} = mC$ of the $\overline{\Delta T}_{max}$ vs C plot at fixed d = 420 μm and ω = 30 μm in the 0–10 K range; m = 254 K/M. (e) Ratio $\overline{\Delta T}_{max}/\Delta T$ of the PSF-convoluted and pixel-averaged temperature increment $\overline{\Delta T}_{max}$ over the actual temperature increment $\Delta T = T(0, 0, 0, \tau_{on}) - T_0$ predicted by equation (1) at varying beam waist ω in the 10–150 μm range and fixed d = 420 μm, τ_{on} = 0.2 s, P_{eff} = 39 mW, k = 0.9 Wm^{-1} K^{-1}, $D = 5.02 \times 10^{-7}$ m^2/s, ℓ = 20 μm, E = 1,500 M^{-1} cm^{-1}, and ϕ = 0.99. Data refer to $C = 5 \times 10^{-4}$ M (yellow), $C = 3.6 \times 10^{-2}$ M (red), and $C = 7.6 \times 10^{-2}$ M (purple); at higher concentration, ΔT increases and the effect of its average over the camera pixels is reduced with overall higher ratio $\overline{\Delta T}_{max}/\Delta T$.

Results

Super-resolution melanin-based photo-thermal imaging on B16 murine melanoma biopsies

Melanogenesis mainly occurs in melanocytes in the epidermal–dermal junction and provides the skin with ultraviolet-absorbing photo-protective agents: melanin shields the DNA of epidermal cells from the direct action of UV light, and scavenges the reactive oxygen species (ROS) associated with UV-induced oxidative stress [33]. Such a photo-protective ability of melanin pigments originates from a monotonically decreasing absorption spectrum in the 300–1,100 nm range [34,35]. Importantly, with a relatively low fluorescence quantum yield [34] upon one- and two-photon excitation, both eu- and pheo-melanins display a highly efficient thermal relaxation upon visible to near-infrared light absorption [5,36], and can be conveniently detected by photo-activated infrared thermography in label-free configuration.

We take advantage here of unstained excised murine B16 melanoma biopsies, and we prime the photo-thermal effect of melanin pigments at the 514 nm wavelength of a low-power Argon laser beam (P_0 = 33 mW on the sample plane). Aiming at achieving the tens-of-μm resolution

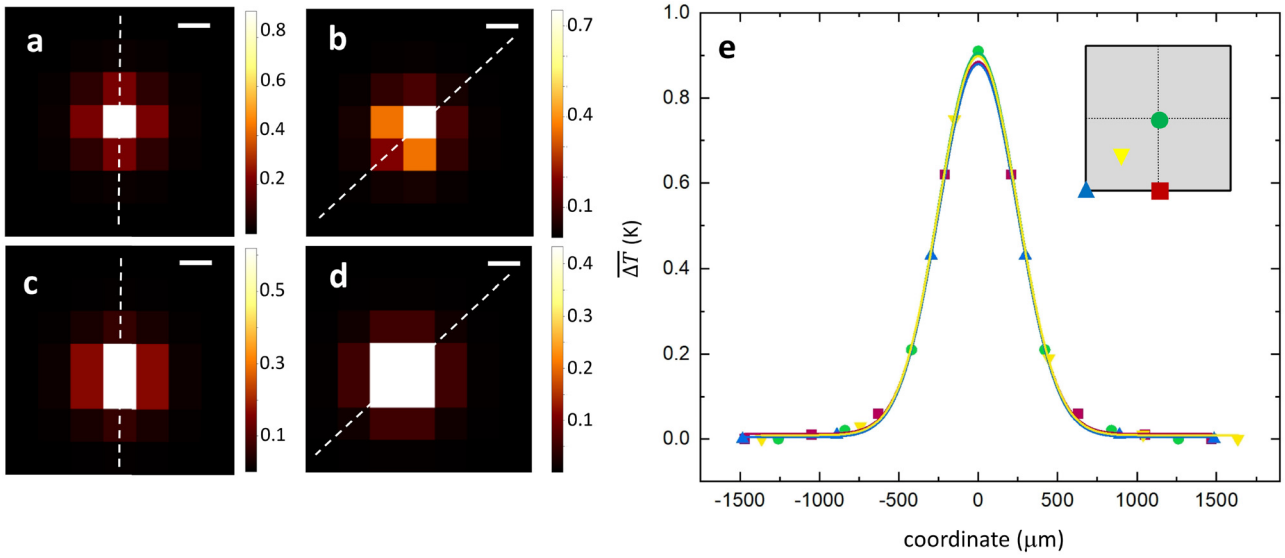

Figure 4: Camera-based detection of temperature increments. (a)–(d) Thermal-camera frame simulated by spatially averaging a PSF-convoluted (and fourth-power elevated) temperature distribution over a fixed grid of adjacent pixels with 420-μm pixel size (ω = 30 μm, 1-mW absorbed power, τ_{on} = 0.2 s, k = 0.9 $Wm^{-1}K^{-1}$, $D = 5.02 \times 10^{-7}$ m^2/s); panels (a)–(d) differ for the peak location of the underlying temperature distribution, which is located at the center of a camera pixel in (a), halfway between the pixel center and the pixel corner in (b), on top of the pixel lower edge in (c), and on the lower-left pixel corner in (d). The four temperature peak locations inside the camera pixel are schematically marked in green, yellow, red, and blue, respectively, in the inset of panel (e). Scale bar = 420 μm for (a)–(d); color bars code for temperature in K. (e) Symbols: pixel-averaged temperature values extracted along the dashed lines in (a)–(d); colors code for the position of the temperature peak as defined in the inset. Continuous lines: best fits of pixel-averaged temperature profiles to a Gaussian function.

that is required by the characterization of the melanin spatial distribution across extended (mm^2–cm^2 sized) tissue sections, we employ our super-resolution image acquisition scheme and reconstruct the thermal image of whole tissue sections by the *a-posteriori* centroid localization of sequences of laser-induced temperature increments [14] (Section 2). We adopt a 30-μm $1/e^2$ excitation beam waist and a laser activation time τ_{on} = 200 ms, leading to typical detected temperature increments in the 0–10 K range. The amplitude and the signal-to-noise ratio associated to these temperature variations allow the identification of their centroid peak coordinates with a 10–50 μm localization uncertainty [14], which is sufficiently high to highlight the spatial heterogeneities in the tissue pigmentation. The reconstructed spatial distribution of melanin pigments is in fact highly non-homogeneous as we demonstrate with the exemplary super-resolution photo-thermal image of a B16 biopsy in Figure 1a. The comparison with the transmitted-light image of the same biopsy, reported in Figure 1b, confirms that the sample morphology is correctly reconstructed and qualitatively highlights that those regions exhibiting more intense heat release are associated to lower light transmission, as expected in the presence of more pronounced pigmentation.

It is finally worth remarking that the adopted super-resolution image acquisition scheme provides a nearly twenty times resolution enhancement [14] relative to the mm-sized resolution of our thermal camera in conventional operation. structures that are clearly resolved in the super-resolution image of Figure 1a would appear therefore indiscernible in the conventional thermal image of the same sample.

From super-resolution photo-thermal imaging to the space-resolved quantification of photo-thermal probes: theoretical framework and experimental guidelines

Besides providing the necessary protection against ultraviolet radiation and reactive oxygen species in the skin, melanin acts as a marker for melanocytes differentiation [26]. It also plays a highly debated regulatory role in cancer evolution, by both decreasing the efficacy of anti-tumor treatments [27] (radio- and chemo-therapy) and by favoring tumor progression with immunosuppressive and mutagenic properties [25,26]. Recent findings [24,37] have

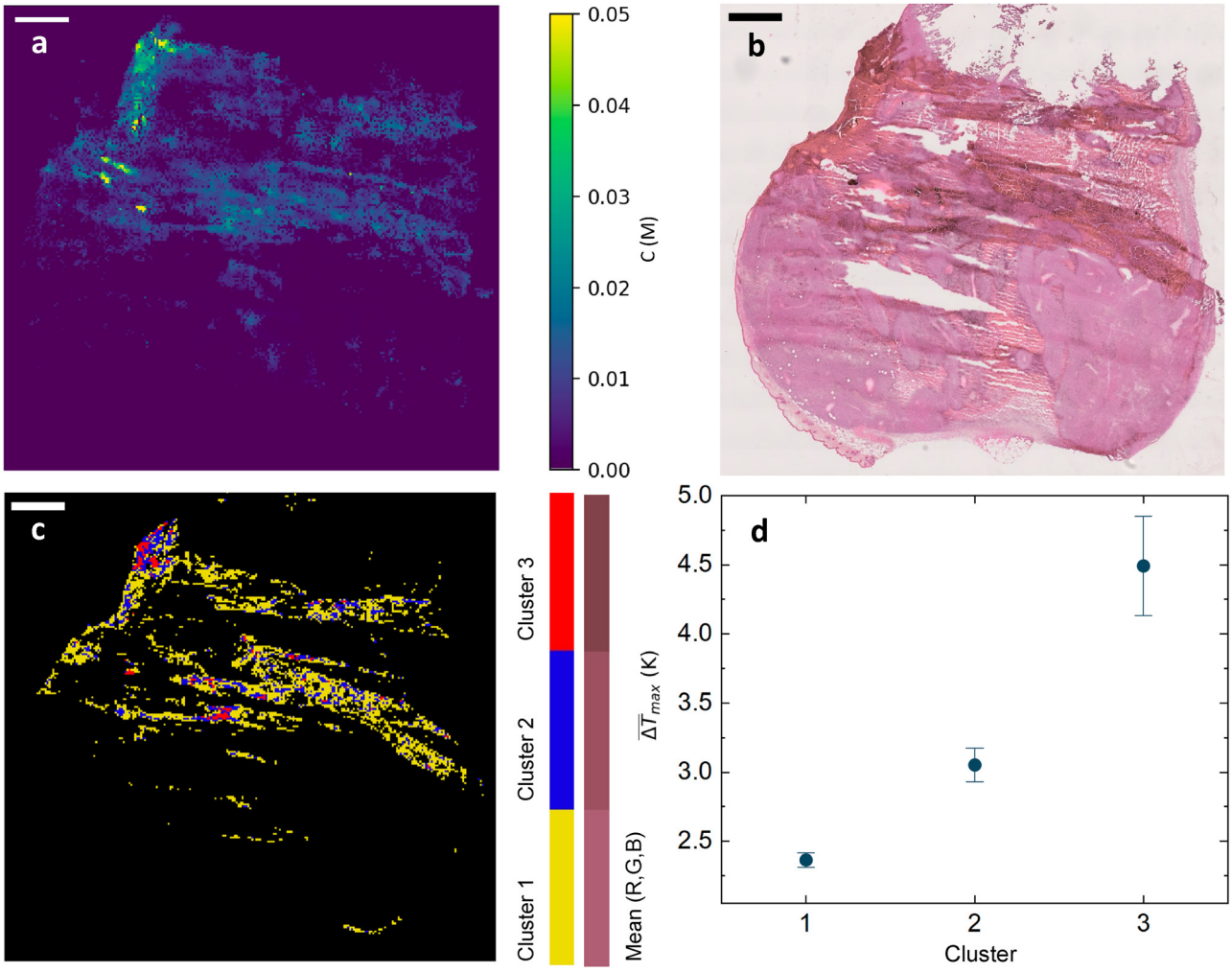

Figure 5: Quantification of the melanin concentration. (a) Super-resolution image of the absolute melanin molar concentration C retrieved from Figure 1a by the pixel-wise conversion $C = \overline{\Delta T}_{max}/m$ (m = 254 K/M). (b) H&E image of the same biopsy imaged in Figure 1a and b. The H&E staining has been performed upon completion of super-resolution thermal imaging experiments on the unstained biopsy. (c) Results of our 2-means lightness-driven clustering applied to the H&E image of panel (b). Pixels in clusters 1, 2, and 3 (color-coded in yellow, blue, and red, respectively) have been selected by three consecutive iterations right before convergence (note that cluster 1 contains clusters 2 and 3, and cluster 2 contains cluster 3), and are associated with increasingly low mean (R,G,B) values: $\bar{R}$ = 162 ± 7, $\bar{G}$ = 98 ± 4, $\bar{B}$ = 115 ± 8 for cluster 1, $\bar{R}$ = 145 ± 7, $\bar{G}$ = 86 ± 4, $\bar{B}$ = 97 ± 7 for cluster 2, and $\bar{R}$ = 119 ± 14, $\bar{G}$ = 69 ± 8, $\bar{B}$ = 75 ± 10 for cluster 3. The corresponding mean ($\bar{R}$, $\bar{G}$, $\bar{B}$) colors are shown in the right color-bar for visual reference. (c) Average amplitude $\overline{\Delta T}_{max}$ of the temperature increments measured in those pixels of Figure 1a classified as belonging to cluster 1 (left), cluster 2 (center), and cluster 3 (right); error bars correspond to the 95% confidence interval.

also suggested that melanin granules may change cell elasticity, thereby modifying cell migration parameters which in turn play a key role in the process of metastasis of malignant melanoma. The quantification of melanin pigments in skin tissues and melanoma biopsies is regarded therefore as a potential diagnostic tool, and the melanin concentration has been suggested [25,28] as a useful parameter to be added to the standard reports of histopathological analyses to complement the morphological/immunohistochemical features traditionally extracted from the visual inspection of (H&E stained) melanocytic lesions *ex-vivo*.

In this framework, we outline the theoretical formalism to extract the absolute molar concentration of melanin pigments from super-resolved photo-thermal images of melanoma biopsies. While we exploit the concentration of melanin as a biologically relevant case study, we provide the readers with theoretical and experimental guidelines that have general validity in the conversion of temperature-based maps into quantitative images of the concentration C of photo-thermal laser-excited probes.

In order to extract quantitative information from detected $\overline{\Delta T}_{max}$ values, it is necessary to elucidate the

explicit dependence of spatio–temporal temperature profiles on C via the solution of the three-dimensional heat transfer equation in the presence of square wave laser light illumination [20] (i.e., of a Gaussian laser beam centered at (0,0,0), having power P_0 and $1/e^2$ radius ω on the sample plane). In the present case the sample consists of a two-layer material composed of a 1 mm thick glass slide and a 20 μm tissue section. It is intuitive that the tissue layer induces light absorption with absorbance A (no light absorption and heat release are observed for a 1 mm glass slide at the adopted incident laser power), whereas the system thermal response is dominated by the underlying thick glass layer. As verified by finite element simulations (Section 2) and as reported in Figure 2, the two-layer system can be modeled as an effective single layer having thickness L = 1,020 μm and with the thermal conductivity and thermal diffusivity of the glass slide. The effect of the lower thermal conductivity of the surface tissue layer can be simply accounted for by rescaling the incident laser power P_0 to an increased value $P_{\text{eff}} = 1.2P_0$, with the necessary 20% power increase estimated by finite element simulations based on the known thermal conductivities (0.37 and 0.9 $\text{Wm}^{-1}\,\text{K}^{-1}$) of skin and glass, respectively (Figure 2).

Under the single-layer approximation, the temperature $T(\boldsymbol{r}, t)$ of the thermally thick sample induced by a square wave laser pulse lasting for τ_{on} [15,16,20] can be formally expressed as

$$T(x, y, z, t) \approx \frac{P_0(1 - e^{-2.303EC\ell})2D\phi}{\pi k} \int_{t_0}^{t} \mathrm{d}t_1 \frac{1}{\omega^2 + 8Dt_1} \exp\left(-\frac{2(x^2 + y^2)}{\omega^2 + 8Dt_1}\right) \times \frac{1}{\sqrt{\pi D t_1}} \exp\left(-\frac{z^2}{4Dt_1}\right) + T_0, \quad (1)$$

where $t_0 = 0$ if $t < \tau_{\text{on}}$ and $t_0 = t - \tau_{\text{on}}$ if $t \geq \tau_{\text{on}}$; T_0 is the ambient temperature, D is the sample thermal diffusivity, and ϕ is the sample thermal relaxation efficiency, which equals here $\phi = 0.99$ for melanin [36]. By recalling Beer–Lambert's law for the sample absorbance and by assuming that light reflection is negligible with respect to absorption, the term $P_0(1 - e^{-2.303EC\ell})$ provides the laser power absorbed by photo-thermal components with molar extinction coefficient E and having effective molar concentration C inside the volume element defined by the thickness ℓ and the excitation laser beam waist. For melanin, E = 1,500 $\text{M}^{-1}\,\text{cm}^{-1}$ at the 514 nm excitation wavelength [38] and ℓ = 20 μm.

The spatial temperature profile predicted by the numerical integration of equation (1) on a 1,020-μm glass sample at the end of a laser pulse lasting for τ_{on} = 200 ms is reported in Figure 3a. Given the low thermal conductivity and diffusivity values of the glass substrate, the width of the temperature increment primed by a 30-μm excitation beam waist is comparable (even lower) to the camera pixel size on the sample plane (420 μm in our case, evidenced by scale bars in Figure 3a–c). Therefore, when the temperature space-time profile of equation (1) gets imaged by a thermal camera, the temperature increment recovered by a non-linear Gaussian fit of the thermal camera frame at time τ_{on} does not coincide with the value $T(0, 0, 0, \tau_{\text{on}}) - T_0$ expected based on equation (1). Experimental data can only be described by convoluting the fourth power of the temperature profile $T(x, y, z, t)$ (which is sensed by the thermal camera according to Stefan–Boltzmann's law) with the camera PSF, and by averaging the resulting distribution over the camera pixelated detector. The peak amplitude of experimentally measured temperature increments should therefore be expressed as

$$\overline{\Delta T}_{\max} = \left\{ \frac{1}{d^2} \int_{-d/2}^{d/2} \int N \cdot [T^4(x, y, 0, \tau_{\text{on}}) \star G(x, y)] \mathrm{d}x \mathrm{d}y \right\}^{1/4} - T_0, \quad (2)$$

where d is the camera pixel size on the sample plane and $N = \int\int_{-\infty}^{+\infty} T^4(x, y, 0, \tau_{\text{on}}) \mathrm{d}x\ \mathrm{d}y / \int\int_{-\infty}^{+\infty} [T^4(x, y, 0, \tau_{\text{on}}) \star G(x, y)] \mathrm{d}x\ \mathrm{d}y$ is the convolution normalization factor. $G(x, y)$ is the camera PSF, which is explicitly approximated to a Gaussian function with unit amplitude and full-width-at-half-maximum ζ assigned by Abbe's diffraction law. The notation $\overline{\Delta T}_{\max}$ will be employed throughout the text to explicitly remark that experimentally measured temperature increments correspond to PSF-convoluted and pixel-averaged values.

When the temperature profile predicted by equation (1) in Figure 3a is convoluted with our thermal-camera PSF, having ζ = 265 μm (Section 2), the temperature profile broadens in space with a corresponding decrease in the peak amplitude (Figure 3b). The spatial average of the resulting temperature distribution over square thermocamera pixels further decreases the signal amplitude and leads to the thermal image reported in Figure 3c. The comparison of Figure 3a and c clearly highlights the importance of properly accounting for the PSF convolution and for the pixelated camera detection when quantitatively describing the experimental temperature values.

By the substitution of equation (1) into equation (2) and by the numerical integration over both space and time, the dependence of $\overline{\Delta T}_{\max}$ on the concentration C of the laser-excited photo-thermal probe can be evaluated. Results are reported in Figure 3d, where the $\overline{\Delta T}_{\max}$ vs C dependence is investigated at fixed camera pixel size

d = 420 µm and varying excitation beam waist ω in the 10–150 µm range. For our 0–10 K typical experimentally measured temperature values (Figure 1a), the combination of a 420-µm pixel size and a 30-µm beam waist leads to a linear dependence of $\overline{\Delta T}_{max}$ on the concentration C (inset in Figure 3d) of the type $\overline{\Delta T}_{max} = mC$ with slope m = 254 K/M. Super-resolved photo-thermal images of melanoma biopsies can be therefore converted into quantitative maps of the absolute molar concentration of melanin pigments by a pixel-wise computation of concentration values according to $C = \overline{\Delta T}_{max}/m$. The lower limit of detection, which depends on the slope m and on the sensitivity of the employed thermal camera, equals in our case C_{min} = 0.1 K/(254 K/M) = 4×10^{-4} M, corresponding to a 0.07 mg/mL concentration based on the eumelanin molar mass of 171 g/mol [39].

According to the results of Figure 3d, the beam waist of the excitation laser beam has been adjusted to 30 µm in all the super-resolution thermal imaging experiments of the present work. Whenever the beam waist is reduced or increased, the dependence of $\overline{\Delta T}_{max}$ on C turns non-linear even in the limited 0–10 K range (Figure 3d), provided that no analytical expression of the $\overline{\Delta T}_{max}$ vs C plot can be recovered (integrals in equations (1) and (2) could not be solved analytically), this non-linearity demands for the identification of a more complicated empirical expression to convert $\overline{\Delta T}_{max}$ into C values.

Besides offering the advantage of a linear $\overline{\Delta T}_{max}$ vs C plot, the combination of 30-µmwaist and 420-µm pixel size allows avoiding laser-induced photo-damage of the sample, while maintaining a sufficiently high signal-to-noise ratio in the acquired thermo-camera images. The ratio $\overline{\Delta T}_{max}/\Delta T$ of the PSF-convoluted and pixel-averaged temperature increment $\overline{\Delta T}_{max}$ over the actual temperature variation $\Delta T = T(0, 0, 0, \tau_{on}) - T_0$ predicted by equation (1) decreases indeed at decreasing waist ω (Figure 3e), pointing out that at fixed $\overline{\Delta T}_{max}$, smaller beam waists require higher excitation laser intensities. At ω = 30 µm, the measured $\overline{\Delta T}_{max}$ values are sufficiently high to reconstruct the melanin distribution at ~40 µm resolution, and no sample photo-damage occurs as verified by sequential transmitted-light imaging on B16 biopsies before and right after photo-thermal imaging experiments (data not shown). Based on the overall results of Figures 1a and 3d–e, the 30-µm waist provides the best compromise to optimize the achievable resolution and simultaneously retrieve the absolute melanin concentration without sample damage with our thermo-camera with 420-µm pixel size.

We finally remark that equation (2) (and the conclusions drawn in Figure 3) assumes that the laser-induced temperature increment (convoluted with the camera PSF) is spatially averaged across a square pixel that is centered on the temperature peak itself. We now consider the general case of a possible shift between the temperature peak and the pixel center, and evaluate the effect of such a shift on the measured amplitude $\overline{\Delta T}_{max}$.

We focus on three possible positions of the temperature peak, as marked and color-coded in the inset of Figure 4e: we consider (i) the extreme case of a temperature peak centered on the pixel corner, (ii) the intermediate case of a temperature peak centered on the pixel edge, and (iii) the case of a temperature peak centered midway between the pixel center and the pixel corner. For each condition, we generate a simulated camera frame by spatially averaging the PSF-convoluted (and fourth-power elevated) temperature profile over a fixed grid of adjacent pixels having 420 µm side (Figure 4b–d), we perform a Gaussian fit of the temperature distribution in the resulting image, and we compare the retrieved maximum amplitude $\overline{\Delta T}_{max}$ with the one obtained in the ideal case of perfect alignment of the temperature peak with the pixel center (Figure 4e). Even in the most unfavorable case of a temperature profile centered on a pixel corner, the amplitude $\overline{\Delta T}_{max}$ decreases at most by 3% relative to the zero-shift amplitude (Figure 4e). This 3% maximum error in the estimate of experimental temperature values, which is associated with the possible misalignment of laser-primed temperature variations relative to the camera pixel center, translates into a maximum 3% uncertainty on recovered concentration values.

Quantification of the melanin absolute concentration by photo-thermal imaging

According to the results of Figure 3d, the super-resolution photo-thermal image of Figure 1a is converted into a map of the melanin molar concentration C in Figure 5a. Recovered concentration values up to 0.05 M agree with reference literature values for human melanoma and human retinal pigment epithelium *ex-vivo* [40,41].

Melanin specificity in the photo-thermal image of Figures 1a and 5a is ensured by the fact that melanin is the most prominent photo-thermal light absorber in melanoma and skin tissues along with hemoglobin, but the blood content and the impact of blood chromophores are expected to be significantly lower in excised biopsies than in vascularized tissues *in vivo* [42]. Furthermore, provided the 0.99 heat-release efficiency of melanin [36] and that the melanin absorption coefficient is about four times larger than the absorption coefficient of

hemoglobin at 514 nm, the contribution of melanin dominates the detected photo-thermal signal [43].

Further confirmation of our melanin specificity can be achieved by an unsupervised machine learning analysis of the H&E image of the same tissue section. The H&E stain provides a comprehensive picture of the anatomy of a biological tissue with cellular nuclei being stained blue and the cells' cytoplasm/extracellular matrix being stained pink [23]. Melanin is not specifically stained, and instead it appears in B16 melanoma as optically contrasted eumelanosome-like brown to black granules [23,27,44]. The pixel color content has already been exploited in the literature to segment melanin in histopathological images [45]. Here we take advantage of the pixel lightness value, the lightness $L = (R + G + B)/3$ being defined in the HSL (Hue, Saturation, Lightness) color space as the arithmetic mean of the red, green, and blue components [21], and we rely on the expected negative correlation between the pixels' melanin content and the L value. We re-bin the H&E image of the tissue section (Figure 5b) to achieve the same 37.8-μm pixel size of the super-resolved photo-thermal image (Figures 1a and 5a), and by applying a k-means clustering [22] with $k = 2$ (Section 2) we partition the pixels of the binned H&E image into two clusters based on the minimization of the Euclidean distance of the pixels (R,G,B) color from the cluster centroid. Upon convergence, we select the cluster having the lowest average lightness $\bar{L}$ (we discard the other clusters) and repeat the 2-means clustering on it. The whole procedure is iterated, in order to progressively select pixels with lower lightness value and expected higher melanin content; iterations get interrupted (convergence is reached) at the n^{th} step, when the difference in the average lightness of the two clusters does not exceed a minimum required threshold. At this point, all pixels belonging to the cluster surviving the $(n-1)^{\text{th}}$ iteration get segmented in the H&E image in binary code (Section 2).

Results are shown in Figure 5c, where the H&E image of Figure 5b is segmented to highlight the result of three consecutive clustering iterations (clusters 1 to 3, respectively: cluster 3 corresponds to the cluster identified at the $(n-1)^{\text{th}}$ iteration before convergence; cluster 2 corresponds to the cluster identified at the $(n-2)^{\text{th}}$ iteration, and cluster 1 corresponds to the one identified at the $(n-3)^{\text{th}}$ iteration). The average color of each group $(\bar{R}, \bar{G}, \bar{B})$, reported as color bar for visual reference (Figure 5c), decreases from cluster 1 ($\bar{R} = 162 \pm 7$, $\bar{G} = 98 \pm 4$, $\bar{B} = 115 \pm 8$) to cluster 3 ($\bar{R} = 119 \pm 14$, $\bar{G} = 69 \pm 8$, $\bar{B} = 75 \pm 10$) as expected, with the corresponding average cluster lightness $\bar{L}$ decreasing from $\bar{L} = 125 \pm 4$ for cluster 1 to $\bar{L} = 88 \pm 6$ for cluster 3.

If the clustered image of Figure 5c is overlaid to the super-resolution photo-thermal image of the same region (Figure 1a), pixels identified as clusters 1–3, respectively, appear to be associated with increasingly higher average detected temperature increments $\overline{\Delta T}_{\max}$ (Figure 5d) and correspondingly more abundant melanin content. The 95% confidence-interval plot of Figure 5d therefore confirms that temperature increments get detected in those pixels that are more likely to contain melanin pigments according to the lightness-driven clustering of the H&E image.

Of note, our machine learning analysis of the H&E image qualitatively selects melanin-rich regions in the tissue but cannot provide any quantitative information regarding the melanin absolute concentration. The exact functional dependence of the color lightness (or of any other combination of the R, G, B color components) on the pigment concentration is not known a priori, preventing the conversion of clustered maps (like Figure 5c) into images of the melanin relative or absolute concentration. Furthermore, the comparison of Figure 5a and c suggests that the minimum melanin concentration that can be detected is lower for super-resolved thermography, with the pixels corresponding to extremely low temperature increments ($\overline{\Delta T}_{\max}$ values close to 0.1 K thermal camera sensitivity) barely appearing in the clustered image of Figure 5c. The quantification of the concentration itself with ~10^{-4} M lower limit of detection is a significant advantage of super-resolution photo-thermal imaging over the employed 2-means clustering on the H&E stain.

Discussion

In summary, we have reported the theoretical foundations of a data acquisition and analysis protocol that enables the space-resolved quantification of the absolute molar concentration of photo-thermal biomarkers in biological tissues by means of super-resolution photo-activated thermal imaging. We have further provided the demonstration of the experimental applicability of the proposed approach on murine B16 melanoma biopsies, where melanin pigments have been spatially mapped at sub-diffraction resolutions over whole (mm^2–cm^2) tissue sections and quantified with 10^{-4} M concentration sensitivity.

Our data acquisition and analysis protocol does not necessarily require single-layer thermally thick slabs, and can be applied to opaque thermally thin samples with surface light absorption by the only adaption of the solution of the 3D heat equation in Equation 1 [20].

Furthermore, super-resolved thermography can be applied to endogenous photo-thermal entities in label-free configuration, as demonstrated here with melanin pigments in melanoma biopsies, as well as to exogenous photo-thermal markers, these can be quantified given the knowledge of their heat release efficiency and molar extinction coefficient. Reflectance properties should also be accounted for in equation (1) whenever light scattering is not negligible with respect to light absorption. The approximation of negligible scattering by melanin pigments is suggested in the literature for dilute melanin solutions [46], and might represent a major source of uncertainty on recovered concentration values in the presence of pigment aggregation.

A general source of uncertainty on measured concentrations can be identified in the assumption of uniform absorption coefficient of photo-thermal probes inside the excitation laser spot. In practical terms, the detected laser-primed photo-thermal signal is interpreted here (equations (1) and (2)) as originating from a spatially uniform distribution of photo-thermal entities with effective concentration C across the laser spot. The spot size provides indeed the bottleneck to the achievable resolution, and we are actually blind to the exact spatial distribution of melanin pigments inside it. In the presence of a space-varying (here Gaussian) laser intensity profile, the fact that the exact distribution of photo-thermal entities inside the laser spot is inaccessible translates into an uncertainty on recovered concentration values, and this uncertainty would turn especially relevant in the presence of extremely sparse photo-thermal chromophores, down to the extreme limit of one melanocyte per excitation spot. We reason a feasible strategy to overcome and mitigate the uncertainty on concentration measurements would consist in replacing the Gaussian-shaped beam profile with a flat-top beam by the inclusion of a Spatial Light Modulator in the excitation optical path. Under this condition, equation (1) should be modified to account for the different illumination profile but equal weight would be given to all photo-thermal entities irrespective of their exact position inside the laser spot.

Our application to melanocytic lesions exemplifies the biological and biomedical relevance of our work, but also implies a broader technological and instrumental impact. From the biomedical point of view, melanin has already been suggested as an important marker for melanoma diagnosis [25,28] but its quantification is not routinely performed in standard histopathological and immunohistochemical analyses of pigmented lesions *ex-vivo*. Existing techniques either rely on cell extracts to quantify melanin pigments with no spatial resolution [44,47,48], or spatially map melanin with no quantification of its concentration [3,5,28,49–51]. Difficulties in tackling the pigment concentration also affect the well-established Fontana-Masson method [52,53] and formalin-fixed paraffin-embedded melanin specific exogenous stains (e.g., melanoma-black-45, S-100, and Melan-A). The thermal imaging approach presented here combines tissue imaging at sub-diffraction resolution with the quantification of the melanin molar content and, by operating in label-free configuration without sample photo-damage, it can be efficiently combined with a subsequent H&E analysis of the same tissue sections. We expect therefore melanin-based super-resolution active thermal imaging to significantly expand the capability of state-of-the-art thermography in complementing standard histopathology in the characterization of biological tissues *ex-vivo*.

From the instrumental and technological point of view, super-resolution thermography can be exploited even in the presence of thermal cameras with smaller pixel size and higher nominal resolution. Commercially available cameras achieving ~20-μm resolution typically operate with costly macro-optics in the mid-infrared spectral band. the number of thermal photons emitted by samples close to ambient temperature is lower than in the far-infrared region, but the photon loss is compensated by an increased camera sensitivity. In the presence of such thermal cameras, the theoretical diffraction barrier can still be overcome by further reducing the laser beam waist down to the sub-micrometer size allowed by visible excitation wavelengths. The combination of our raster-scanning super-resolution image acquisition with mid-infrared cameras could push therefore temperature mapping down to the sub-cellular scale.

We conclude by remarking that a final technological improvement over the results presented here would involve a reduction in the imaging time, which is currently limited in the hours range due to the intrinsically time-consuming procedure of sample illumination and temperature localization. Possible strategies to reduce the total data acquisition time include the implementation of multi-spot laser illumination and the exploitation of sparsity-based data analysis algorithms recently proposed for super-resolution infrared thermography and capable of yielding faster results than the Gaussian image fitting exploited here [54].

Funding information: The authors acknowledge funding from the European Union's Horizon 2020 research and innovation programme under grant agreement No. 964481 (FET Open project "IN2SIGHT"). The authors also acknowledge funding (2018-ATE-0070 and 2019-ATE-0126) from Università degli Studi di Milano-Bicocca.

Conflict of interest: The authors declare no conflicts of interest.

Data availability statement: The datasets generated during and/or analyzed during the current study are available from the corresponding author upon reasonable request.

References

[1] Okabe K, Inada N, Gota C, Harada Y, Funatsu T, Uchiyama S. Intracellular temperature mapping with a fluorescent polymeric thermometer and fluorescence lifetime imaging microscopy. Nat Commun. 2012;3:705.

[2] Herman C. The role of dynamic infrared imaging in melanoma diagnosis. Expert Rev Dermatol. 2013;8:177–84.

[3] He J, Wang N, Tsurui H, Kato M, Iida M, Kobayashi T. Noninvasive, label-free, three-dimensional imaging of melanoma with confocal photothermal microscopy: Differentiate malignant melanoma from benign tumor tissue. Sci Rep. 2016;6:30209.

[4] Lapierre-Landry M, Gordon AY, Penn JS, Skala MC. *In vivo* photothermal optical coherence tomography of endogenous and exogenous contrast agents in the eye. Sci Rep. 2017;7:9228.

[5] Kobayashi T, Nakata K, Yajima I, Kato M, Tsurui H. Label-free imaging of melanoma with confocal photothermal microscopy: Differentiation between malignant and benign tissue. Bioengineering. 2018;5:67.

[6] Miyazaki J, Kobayahsi T. Photothermal microscopy for high sensitivity and high resolution absorption contrast imaging of biological tissues. Photonics. 2017;4(32):1–12.

[7] Donner JS, Thompson SA, Kreuzer MP, Baffou G, Quidant R. Mapping intracellular temperature using green fluorescent protein. Nano Lett. 2012;12:2107–11.

[8] Farzaneh M, Maize K, Lüeren D, Summers JA, Mayer PM, Raad PE, et al. CCD-based thermoreflectance microscopy: Principles and applications. J Phys D Appl Phys. 2009;42:143001.

[9] Vollmer M, Möllmann KP. Infrared thermal imaging: Fundamentals, research and applications. NJ, USA: Wiley-Vch; 2017.

[10] Usamentiaga R, Venegas P, Guerediaga J, Vega L, Molleda J, Bulnes FG. Infrared thermography for temperature measurement and non-destructive testing. Sensors. 2014;14:12305–48.

[11] Pirtiniçetingl M, Herman C. Quantification of the thermal signature of a melanoma lesion. Int J Therm Sci. 2011;50:421–31.

[12] Okabe T, Fujimura T, Okajima J, Kambayashi Y, Aiba S, Maruyama S. First-in-human clinical study of novel technique to diagnose malignant melanoma via thermal conductivity measurements. Sci Rep. 2019;9:3853.

[13] Thang DC, Wang Z, Lu X, Xing B. Precise cell behaviors manipulation through light-responsive nano-regulators: Recent advance and perspective. Theranostics. 2019;9:3308–40.

[14] Bouzin M, Marini M, Zeynali A, Borzenkov M, Sironi L, D'Alfonso L, et al. Photo-activated raster scanning thermal imaging at sub-diffraction resolution. Nat Commun. 2019;10:1–9.

[15] Marini M, Bouzin M, Sironi L, D'Alfonso L, Colombo R, Di Martino D, et al. A novel method for spatially-resolved thermal conductivity measurement by super-resolution photo-activated infrared imaging. Mater Today Phys. 2021;18:100375.

[16] Bouzin M, Marini M, Chirico G, Granucci F, Mingozzi F, Colombo R, et al. Melanin concentration maps by label-free super-resolution photo-thermal imaging on melanoma biopsies. Biomed Opt Exp. 2022;13:1173.

[17] Hecht E. Optics. MA, USA: Addison-Wesley; 2001.

[18] Abbe E. Beiträge zur. Theorie des. Mikrosk. und der mikroskopischen Wahrnem. Arch für Mikroskopische Anat. 1873;9:413–68.

[19] Graciani G, Amblard F. Super-resolution provided by the arbitrarily strong superlinearity of the blackbody radiation. Nat Commun. 2019;10.

[20] Bäuerle D. Laser processing and chemistry. Germany (Springer Berlin Heidelberg): Springer; 2011.

[21] Saravanan G, Yamuna G, Nandhini S. Real time implementation of RGB to HSV/HSI/HSL and its reverse color space models. In 2016 International Conference on Communication and Signal Processing (ICCSP). 2016. p. 462–6.

[22] Hartigan JA, Wong MA. Algorithm AS 136: A *K*-means clustering algorithm. J. R. Stat. Soc. Ser. C. (Appl. Stat). 1979;28:100–8.

[23] Chan JKC. The wonderful colors of the hematoxylin-eosin stain in diagnostic surgical pathology. Int J Surg Pathol. 2014;22:12–32.

[24] Sarna M, Krzykawska-Serda M, Jakubowska M, Zadlo A, Urbanska K. Melanin presence inhibits melanoma cell spread in mice in a unique mechanical fashion. Sci Rep. 2019;9:1–9.

[25] Slominski RM, Zmijewski MA, Slominski AT. The role of melanin pigment in melanoma. Exp Dermatol. 2015;24:258–9.

[26] Brozyna AA, Jóźwicki W, Carlson JA, Slominski AT. Melanogenesis affects overall and disease-free survival in patients with stage III and IV melanoma. Hum Pathol. 2013;44:2071–4.

[27] Brozyna AA, Józwicki W, Roszkowski K, Filipiak J, Slominski AT. Melanin content in melanoma metastases affects the outcome of radiotherapy. Oncotarget 2016;7:17844–53.

[28] Matthews TE, Piletic IR, Selim MA, Simpson MJ, Warren WS. Pump-probe imaging differentiates melanoma from melanocytic nevi. Sci Transl Med. 2011;3.

[29] Betzig E, Patterson GH, Sougrat R, Lindwasser OW, Olenych S, Bonifacino JS, et al. Imaging intracellular fluorescent proteins at nanometer resolution. Sci. (80-). 2006;313:1642–5.

[30] Rust MJ, Bates M, Zhuang X. Sub-diffraction-limit imaging by stochastic optical reconstruction microscopy (STORM). Nat Methods. 2006;3:793–5.

[31] Bernard V, Staffa E, Mornstein V, Bourek A. Infrared camera assessment of skin surface temperature - Effect of emissivity. Phys Medica. 2013;29:583–91.

[32] Ogi H, Ishihara T, Ishida H, Nagakubo A, Nakamura N, Hirao M. Thermal Mode Spectroscopy for Thermal Diffusivity of Millimeter-Size Solids. Phys Rev Lett. 2016;117:195901.

[33] Solano F. Photoprotection and skin pigmentation: melanin-related molecules and some other new agents obtained from natural sources. Molecules. 2020;25(1537):1–18.

[34] Fu D, Ye T, Matthews TE, Yurtsever G, Warren WS. Two-color, two-photon, and excited-state absorption microscopy. J Biomed Opt. 2007;12:054004.
[35] Sun C-K, Wu P-J, Chen S-T, Su Y-H, Wei M-L, Wang C-Y, et al. Slide-free clinical imaging of melanin with absolute quantities using label-free third-harmonic-generation enhancement-ratio microscopy. Biomed Opt Exp. 2020;11:3009.
[36] Meredith P, Riesz J. Radiative relaxation quantum yields for synthetic Eumelanin. Photochem Photobiol. 2004;79:211.
[37] Sarna M, Zadlo A, Hermanowicz P, Madeja Z, Burda K, Sarna T. Cell elasticity is an important indicator of the metastatic phenotype of melanoma cells. Exp Dermatol. 2014;23:813–8.
[38] Ansari MA, Mohajerani E. Mechanisms of laser-tissue interaction: I. Optical properties of tissue. J Lasers Med Sci. 2011;2:119–25.
[39] Piletic IR, Matthews TE, Warren WS. Estimation of molar absorptivities and pigment sizes for eumelanin and pheomelanin using femtosecond transient absorption spectroscopy. J Chem Phys. 2009;131:1–4.
[40] Shu X, Li H, Dong B, Sun C, Zhang HF. Quantifying melanin concentration in retinal pigment epithelium using broadband photoacoustic microscopy. Biomed Opt Exp. 2017;8:2851.
[41] Morishima T, Fukuda E. Quantitative analysis of eumelanin and pheomelanin in human malignant-melanoma tissues. Arch Dermatol Res. 1985;277:248–50.
[42] Hult J, Merdasa A, Pekar-Lukacs A, Tordengren Stridh M, Khodaverdi A, Albinsson J, et al. Comparison of photoacoustic imaging and histopathological examination in determining the dimensions of 52 human melanomas and nevi *ex vivo*. Biomed Opt Exp. 2021;12:4097.
[43] Meglinski I V, Matcher SJ. Quantitative assessment of skin layers absorption and skin reflectance spectra simulation in the visible and near-infrared spectral regions. Physiol Meas. 2002;23:741–53.
[44] Ito S, Jimbow K. Quantitative analysis of eumelanin and pheomelanin in hair and melanomas. J Invest Dermatol. 1983;80:268–72.
[45] Kłeczek P, Lech M, Jaworek-Korjakowska J, Dyduch G, Tadeusiewicz R. Segmentation of black ink and melanin in skin histopathological images. Proc SPIE. 2018;10581:335–42. doi: 10.1117/12.2292859.
[46] Riesz J, Gilmore J, Meredith P. Quantitative scattering of melanin solutions. Biophys J. 2006;90:4137–44.
[47] Chung S, Lim GJ, Lee JY. Quantitative analysis of melanin content in a three-dimensional melanoma cell culture. Sci Rep. 2019;9:1–9.
[48] Fernandes B, Matamá T, Guimarães D, Gomes A, Cavaco-Paulo A. Fluorescent quantification of melanin. Pigment Cell Melanoma Res. 2016;29:707–12.
[49] Dimitrow E, Riemann I, Ehlers A, Koehler MJ, Norgauer J, Elsner P, et al. Spectral fluorescence lifetime detection and selective melanin imaging by multiphoton laser tomography for melanoma diagnosis. Exp Dermatol. 2009;18:509–15.
[50] Fu D, Ye T, Matthews TE, Grichnik J, Hong L, Simon JD, et al. Probing skin pigmentation changes with transient absorption imaging of eumelanin and pheomelanin. J Biomed Opt. 2008;13:054036.
[51] He J, Miyazaki J, Wang N, Kobayashi T. Label-free imaging of melanoma with nonlinear photothermal microscopy. Opt Lett. 2015;40:1141–4.
[52] Joly-Tonetti N, Wibawa JID, Bell M, Tobin D. Melanin fate in the human epidermis: a reassessment of how best to detect and analyse histologically. Exp Dermatol. 2016;25:501–4.
[53] Carriel VS, Aneiros-Fernandez J, Arias-Santiago S, Garzón IJ, Alaminos M, Campos A. A novel histochemical method for a simultaneous staining of melanin and collagen fibers. J Histochem Cytochem. 2011;59:270–7.
[54] Burgholzer P, Berer T, Gruber J, Mayr G. Super-resolution thermographic imaging using blind structured illumination. Appl Phys Lett. 2017;111:031908.